JACS
JOURNAL OF THE AMERICAN CHEMICAL SOCIETY
Article
pubs.acs.org/JACS

Enhanced Photochemical Hydrogen Evolution from Fe_4S_4-Based Biomimetic Chalcogels Containing M^{2+} (M = Pt, Zn, Co, Ni, Sn) Centers

Yurina Shim,[†] Ryan M. Young,[†] Alexios P. Douvalis,[‡] Scott M. Dyar,[†] Benjamin D. Yuhas,[†] Thomas Bakas,[‡] Michael R. Wasielewski,[†] and Mercouri G. Kanatzidis*[,†]

[†]Department of Chemistry and Argonne-Northwestern Solar Energy Research (ANSER) Center, Northwestern University, Evanston, Illinois 60208, United States

[‡]Department of Physics, University of Ioannina, 45110 Ioannina, Greece

Supporting Information

ABSTRACT: Naturally abundant enzymes often feature active sites comprising transition metal cluster units that catalyze chemical processes and reduce small molecules as well as protons. We introduce a family of new chalcogenide aerogels (chalcogels), aiming to model the function of active sites and the structural features of a larger protective framework. New metal incorporated iron sulfur tin sulfide chalcogels referred to as ternary chalcogels and specifically the chalcogels M-ITS-cg3, fully integrate biological redox-active Fe_4S_4 clusters into a semiconducting porous framework by bridging them with Sn_4S_{10} linking units. In the M-ITS-cg3 system we can tailor the electro- and photocatalytic properties of chalcogels through the control of spatial distance of redox-active Fe_4S_4 centers using additional linking metal ions, M^{2+} (Pt, Zn, Co, Ni, Sn). The presence of a third metal does not change the structural properties of the biomimetic chalcogels but modifies and even enhances their functional performance. M-ITS-cg3s exhibit electrocatalytic activity in proton reduction that arises from the Fe_4S_4 clusters but is tuned inductively by M^{2+}. The metal ions alter the reduction potential of Fe_4S_4 in a favorable manner for photochemical hydrogen production. The Pt incorporated ITS-cg3 shows the greatest improvement in the overall hydrogen yield compared to the binary ITS-cg3. The ability to manipulate the properties of biomimetic chalcogels through synthetic control of the composition, while retaining both structural and functional properties, illustrates the chalcogels' flexibility and potential in carrying out useful electrochemical and photochemical reactions.

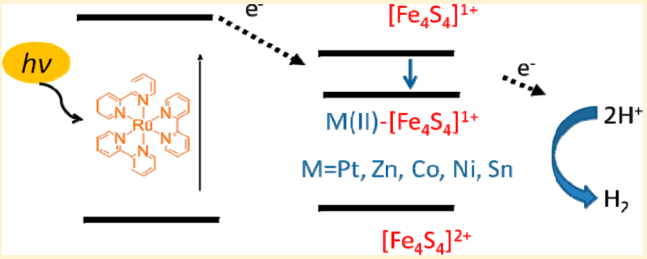

INTRODUCTION

Global research efforts have paid intense attention to hydrogen gas (H_2) as a promising future energy carrier due to its high energy content, minimal environmental impact, and possible direct usage in fuel cells.[1,2] As most hydrogen production techniques require high temperature and pressure conditions, there is strong interest in mild, molecular-based approaches.[3] Meanwhile, nature provides a highly efficient tool for H_2 evolution with proteins called hydrogenases, which are able to convert protons catalytically into molecular hydrogen without the use of extreme conditions.[1] Particularly, in the photosynthesis process, solar energy is collected and stored as chemical energy via catalysis of enzymes including hydrogenase, which utilizes only nickel and/or iron for reversible H_2 evolution/oxidation.[4−10] Although some progress has been made in the development of catalysts that promote the reduction of protons to H_2,[11] powered by a photosensitizer or direct excitation,[12−15] bioinspired systems are emerging as possible alternatives to meet the technological requirements for applications with lower cost because their constituents are often earth-abundant transitional metals such as iron.[16−19]

Biomimetic systems are of interest for modeling the active site of hydrogenase enzymes and aim toward designing suitable catalysts for photochemical hydrogen production.[9,20] The current biomimetic species, which show a comparable catalytic efficiency to the enzyme,[19,21−23] are molecular in nature.[16,24−27] Moreover, many of these biomimetic species exhibit shortened lifetimes,[28−31] and few have shown tunability in performance.[32−34] An attractive strategy for increasing the stability and efficiency of the catalysts is to embed them into a larger robust framework, mimicking the surrounding protein environment in the natural enzymes.[6,35,36]

Efforts in our laboratory have focused on mimicking structural and functional principles of hydrogenases by synthetic chemistry. We have investigated the directed integration of enzyme cofactor analogues into larger artificial porous structures.[37−40] This created the class of chalcogenide aerogels, called biomimetic chalcogels, which provide stable active sites that are readily accessible to substrates.[41] Further,

Received: July 18, 2014
Published: August 27, 2014

dx.doi.org/10.1021/ja507297p | J. Am. Chem. Soc. 2014, 136, 13371−13380

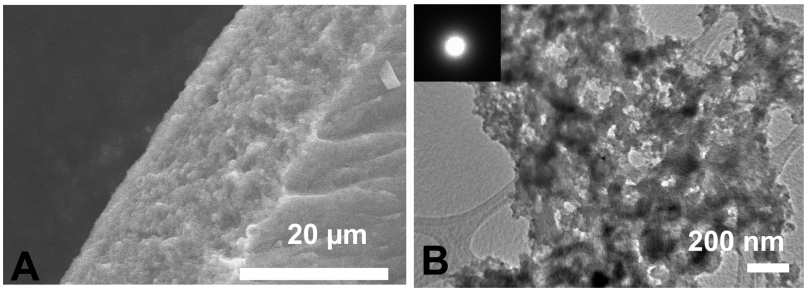

Figure 1. (A) SEM image showing porous nature of Co-ITS-cg3. (B) TEM of Co-ITS-cg3 illustrating the absence of an extended lattice structure. The inset is a representative selected area electron diffraction (SAED) pattern of the chalcogel. All of the M-ITS-cg3s synthesized are similar in appearance (Supporting Information, Figure S1).

the biomimetic chalcogels' high surface areas along with a wide chemical versatility in composition allow for the tunability of the gels in electrochemical and photochemical properties.[42,43]

We have recently introduced the family of iron sulfur tin sulfide chalcogels (ITS-cg) composed of Fe_4S_4 redox-active clusters bridged by thiostannate groups of $[Sn_nS_{2n+2}]^{4-}$, where n = 1, 2, and 4, referred to as ITS-cg1 for n = 1, -cg2 for n = 2, and -cg3 for n = 4. The biomimetic ITS-cgs can be tailored by varying n during a self-assembled synthesis step, which alters the relevant electrochemical redox potential of $[Fe_4S_4]^{2+}$ clusters and changes the electrochemical and photochemical properties of chalcogels.[38] Tuning of the chalcogels' properties is also possible by altering the density of active centers through the addition of third metals in the chalcogel structure. Previously we reported biomimetic chalcogels composed of Fe_4S_4 redox-active centers and metal cations bridged by dimeric $[Sn_2S_6]^{4-}$ units (ITS-cg2) and showed their enhanced electrocatalytic properties.[40]

In efforts to improve the electrochemical properties of chalcogels and further enhance the light-to-hydrogen conversion capability, we prepared a new set of porous ITS-cg3 chalcogels inspired by the heterobimetallic active site in NiFe hydrogenase involving the tetrameric adamantane $[Sn_4S_{10}]^{4-}$ units.[12,19,40] In this report, we describe a second generation of biomimetic chalcogel incorporating a third divalent transition metal cation to binary ITS-cg3, resulting in $\{[Fe_4S_4]_xM^{2+}{}_y[Sn_4Sn_{10}]_z\}$(dubbed as ternary M-ITS-cg3). By introducing a third redox-inactive transition metal into the chalcogel framework, we control the density and spacing of redox-active $[Fe_4S_4]^{2+}$ clusters within the ITS-cg3 structure, which affects the electronic properties of the gels. In addition, we observe cooperative effects between $[Fe_4S_4]$ and the third metal cations reminiscent of those found in the heterometal cluster of hydrogenases.[19,34,44] To enable photocatalytic activity in these systems, we install a light-harvesting molecule using an ion-exchange process that is capable of energy transfer to the catalytic inorganic biomimetic clusters.

We show that redox-inactive metals Ni^{2+}, Co^{2+}, Sn^{2+}, Zn^{2+}, and Pt^{2+} can be coincorporated into ITS-cg3 while maintaining the high surface area and the redox activity of the $[Fe_4S_4]^{2+}$ clusters. These metals strongly affect the electrochemical reduction potentials and electron-transfer processes within the chalcogel framework, ultimately contributing to enhanced light-to-hydrogen conversion capability shown by the dye-functionalized chalcogels, $\{[Fe_4S_4]_xM^{2+}{}_y[Sn_4Sn_{10}]_z[Ru(bpy)_3]_m\}$. Our synthetic route also increases the stability of catalytic centers of the gels, resulting in long-term photochemical activity. We observe that the new ternary M-ITS-cg3s are superior in light-driven H_2 production activity and stability to the previously reported parent ITS-cg3.[38]

RESULTS AND DISCUSSION

Synthesis. M-ITS-cg3 materials were synthesized according to the mixed metathesis reaction of eq 1.

$$x[Fe_4S_4Cl_4]^{2-} + yM^{2+} + z[Sn_4S_{10}]^{4-} \rightarrow \{[Fe_4S_4]_xM_y[Sn_4Sn_{10}]_z\}^{m-} + zCl^-; \quad 2x + 2y = 4z + m \qquad (1)$$

All M-ITS-cg3 materials display the same spongy morphology, and they feature random nonperiodic structures (Figure 1, Scheme 1, Table 1, and Supporting Information, Figure S1).

The metal sulfide networks in the M-ITS-cg3 chalcogels are negatively charged and have countercations such as Ph_4P^+ or $[(CH_3CH_2)_4N]^+$ to be charge-balanced (cations come from precursors). In the case of Pt-containing ITS-cg3 (Pt-ITS-cg3), in addition to K^+ from K_2PtCl_4, excess Pt^{2+} also seems to be present, helping to balance the charge. Elemental analysis of the M-ITS-cg3s shows the existence of countercations, as well as excess Pt^{2+} in Pt-ITS-cg3 (Supporting Information, Table S1). The countercations play a critical role in incorporating the cationic light-harvesting system (to be discussed in detail later) (Supporting Information, Table S1).

The nitrogen adsorption−desorption isotherms of the supercritically dried M-ITS-cg3s exhibit Type IIb behavior, with surface areas ranging from 130 to 260 m^2/g (Figure 2A, Table 1). In addition, the third metal does not appear to prevent the Fe_4S_4 cubane cluster from firmly incorporating into the chalcogel suprastructure. The cubane cluster was identified by thiol-extrusion experiments (Figure 2B and Supporting Information, Figure S2), a well-established method of detecting Fe_4S_4 clusters in their native proteins, as well as Mössbauer spectroscopy (see below).[45] The Fe_4S_4 cluster is extruded from the chalcogel framework when excess thiophenol reacts with the chalcogels in *N,N′*-dimethylformamide, resulting in a brown/black solution. The extruded Fe_4S_4 cluster in the solution is then detected by UV−visible spectroscopy with the maximum absorption at 455 nm, a characteristic peak of $[Fe_4S_4(SPh)_4]^{2-}$.[24,46,47]

Mössbauer Spectroscopy. To characterize the Fe_4S_4 clusters and thiostannate units in the presence of the third transition metal in the ITS-cg3 chalcogels, we used ^{57}Fe and ^{119}Sn Mössbauer spectroscopy, respectively. Given the aperiodic nature of the chalcogels, this technique offers a unique tool to probe the structural and electronic properties of the clusters. ^{57}Fe Mössbauer spectra of the parent ITS-cg3 and

dx.doi.org/10.1021/ja507297p | J. Am. Chem. Soc. 2014, 136, 13371−13380

Scheme 1. Synthetic (A) Scheme and (B) Images of M-ITS-cg3: (A) (TEA = $[(CH_3CH_2)_4N]^+$; M = Pt, Co, Ni, Sn, Zn; L = (O_2CCH_3), Cl, ($O_2C_5H_7$)); Red = M, Yellow = S, Blue = Fe, and Black = Sn; (B) Images of M-ITS-cg3 (1) Before and (2) after Adding M^{2+} Ions, and (3) after the Completion of Gelation

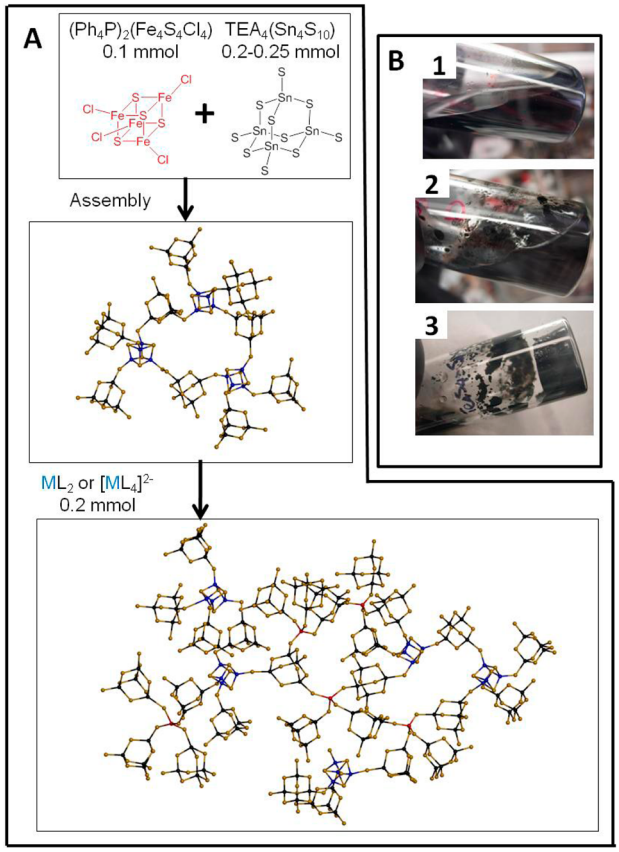

Table 1. Elemental Composition, BET Surface Area, And Electronic Parameter of Binary ITS-cg3 and Ternary M-ITS-cg3 Samples

chalcogel	third metal	observed empirical formula[a]	BET surface area (m^2/g)	first reduction potential[b] (mV)
ITS-cg3		$[Fe_4S_4]_{3.1}[Sn_4S_{10}]_2$	252	−750
Pt-ITS-cg3	Pt	$Pt_{2.8}$ $[Fe_4S_4]_{2.2}[Sn_4S_{10}]_2$	257	−500
Zn-ITS-cg3	Zn	$Zn_{1.3}[Fe_4S_4]_{2.0}[Sn_4S_{10}]_2$	262	−560
Sn-ITS-cg3	Sn	not available[c]	257	−700
Ni-ITS-cg3	Ni	$Ni_{0.7}[Fe_4S_4]_{2.8}[Sn_4S_{10}]_2$	238	−700
Co-ITS-cg3	Co	$Co_{1.7}[Fe_4S_4]_{1.4}[Sn_4S_{10}]_2$	129	−680

[a]Composition normalized to two $[Sn_4S_{10}]$ linking blocks. [b]Refers to Ag/AgCl at room temperature; υ = 0.06 V/s. [c]Accurate empirical formula for the Sn-ITS-cg3 could not be determined because the third metal shares the same element as the Sn_4S_{10} linking units.

all other M-ITS-cg3 chalcogels appear very similar at 77 K (Figure 3A and Supporting Information, Figure S3). At this temperature, all spectra show two main components (green and red colored components; quadrupole doublets) with Mössbauer parameters identifying the Fe_4S_4 clusters (Supporting Information, Table S3).[38] A minor component is also observed corresponding to a small impurity of high-spin (S = 2) Fe^{2+} state (brown colored components in Figure 3 and Supporting Information, Figure S3), originating most probably from unavoidable partial oxidation. In addition, the Sn-ITS-cg3 sample features an extra component (blue-colored component in Supporting Information, Figure S3) with Mössbauer parameters characteristic of iron in the Fe_4S_4 cubane structure but with a higher ΔE_Q value with respect to all other Fe_4S_4 cubane-relative components, suggesting that some of the Fe_4S_4 cubanes in Sn-ITS-cg3 are distorted.[48,49] These results suggest that, for the parent ITS-cg3 sample, as well as all M-ITS-cg3s, the majority of the iron present in them is hosted in the Fe_4S_4 cubane clusters.

The effect of metal addition is especially apparent in Zn-ITS-cg3 when measured at a lower temperature, 10 K. The Zn-ITS-cg3 sample shows a different spectrum from all the other ternary chalcogel samples (Figure 3B and Supporting Information, Figure S3), with the magnetic part of the spectrum at 10 K being close to 100%. This spectrum is similar to the previously studied ITS-cg1 sample, in which Fe_4S_4 clusters are linked by $[SnS_4]^{4-}$ linking units. In ITS-cg1 with $[SnS_4]^{4-}$ being linking units, the closer mutual spatial proximity of Fe_4S_4 cubanes than that in ITS-cg3 promotes magnetic coupling of the Fe_4S_4 units.[38] These ^{57}Fe Mössbauer results suggest that, in Zn-ITS-cg3, the Fe_4S_4 units are closer to each other relative to the other M-ITS-cg3 samples. However, with the ternary metal acting as a spacer between the clusters as discussed below, Zn^{2+} in Zn-ITS-cg3 could also introduce some inductive effects where the magnetic coupling as well as electronic interaction between Fe_4S_4 clusters (i.e., electron hopping) can be achieved more effectively.

The effects of different metals on the properties of M-ITS-cg3 are also observed in the zero-field ^{119}Sn Mössbauer spectra of the corresponding samples collected at 80 K, providing information on the state of the Sn ions (Figure 3C and Supporting Information, Figure S4 and Table S4). The expected characteristics for Sn^{4+} ions in the $[Sn_nS_{2n+2}]^{4-}$ linking blocks are observed in all samples (Supporting Information, Table S4, components I and II). The Pt inclusion results in a spectrum that is quite similar to the one shown by the parent ITS-cg3 (Figure 3C). The Mössbauer spectra for all M-ITS-cg3 samples suggest that the $[Sn_4S_{10}]^{4-}$ linking blocks in M-ITS-cg3 can retain the adamantane structure just as in the parent binary ITS-cg3. However, as evidenced by the relative absorption areas of the standard pair of components (I and II) used to fit the spectra of all samples,[38] the majority of the Sn^{4+} ions in the $[Sn_4S_{10}]^{4-}$ linking blocks appear to correspond to component I and acquire a more symmetric environment for the cases of M-ITS-cg3s (Supporting Information, Table S4). In the case of the Zn-ITS-cg3 spectrum, it is interesting to note that component II of the pair acquires a quite lower ΔE_Q value than all corresponding II components for the other samples, indicating a more symmetric environment for the ligands around the Sn^{4+} ions for this component as well.

The ^{57}Fe and ^{119}Sn Mössbauer spectra suggest that the M-ITS-cg3 chalcogels contain on average more widely spaced $Fe_4S_4/[Sn_4S_{10}]^{4-}$ units than the parent ITS-cg3, which is consistent with the expectation that the added transition metal is acting as a spacer between the units. These results also indicate that the addition of the third metal preserves the structure and nature of the Fe_4S_4 centers; however, their

dx.doi.org/10.1021/ja507297p | J. Am. Chem. Soc. 2014, 136, 13371−13380

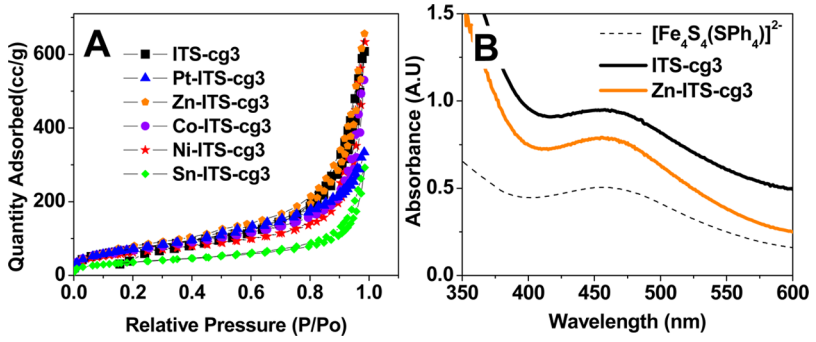

Figure 2. (A) Nitrogen adsorption/desorption isotherm at 77 K of binary and ternary M-ITS-cg3 samples, exhibiting the mixture of meso- and macropore distribution. (B) UV−vis spectra of chalcogel solutions after a thiol-extrusion experiment, reflecting the absorption of the extruded $[Fe_4S_4(SPh_4)]^{2-}$ anion in parent ITS-cg3 and Zn-ITS-cg3. All of the M-ITS-cg3s synthesized display similar spectra (Supporting Information, Figure S2).

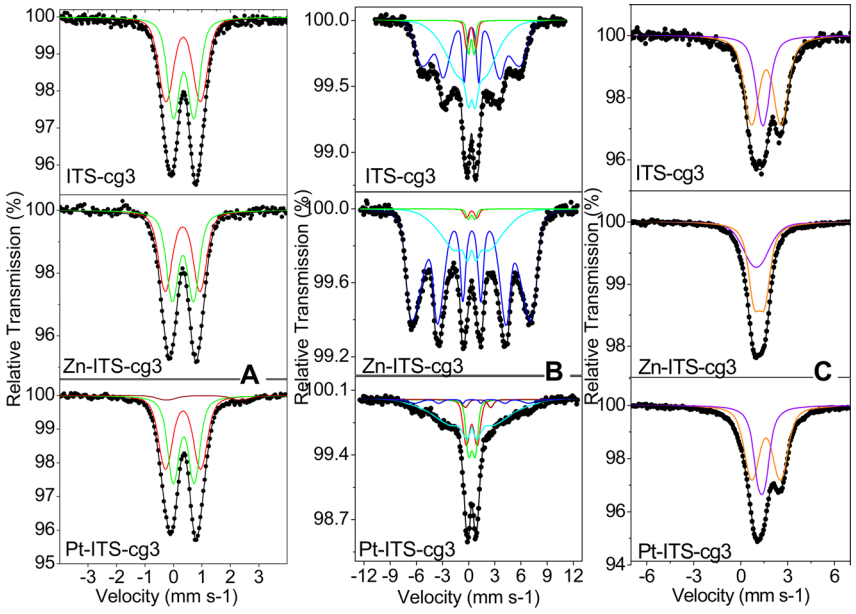

Figure 3. Characteristic ^{57}Fe Mössbauer spectra of parent ITS-cg3, Zn-ITS-cg3, and Pt-ITS-cg3 samples recorded at (A) 77 K and (B) 10 K. All other M-ITS-cg3 chalcogels display similar ^{57}Fe Mössbauer spectra to the parent ITS-cg3 at 77 and 10 K (Supporting Information, Figure S3). (C) Characteristic ^{119}Sn Mössbauer spectra of the ITS-cg3, Zn-ITS-cg3, and Pt-ITS-cg3 samples recorded at 80 K. All other M-ITS-cg3 samples display similar ^{119}Sn Mössbauer spectra to the Zn-ITS-cg3 (Supporting Information, Figure S4). Experimental data are denoted with points, and their deconvolution with the relative components (colored continuous lines) is also shown in each spectrum.

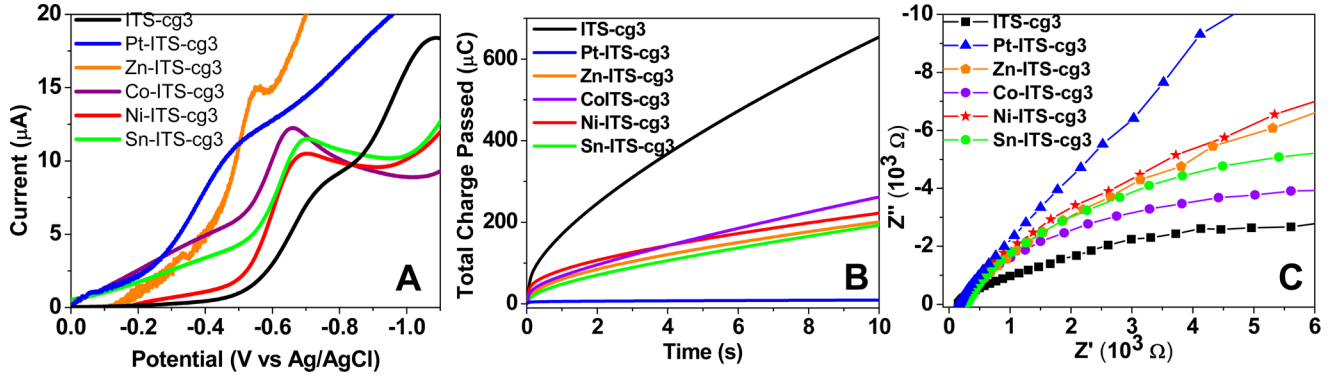

Figure 4. (A) CVs of chalcogels scanned at 0.06 V/s, showing redox activity in M-ITS-cg3 samples and more anodic reduction potentials at M-ITS-cg3 samples. The currents are scaled to fit on a common scale and to display better reduction-peak comparison. Reverse scans of curves have been omitted for clarity. (Full scan in Supporting Information, Figure S5). (B) Chronocoulometry data of chalcogels showing decreased total charge passed in M-ITS-cg3s. (C) Impedance spectra of chalcogels obtained with a constant DC potential of −1000 mV and an amplitude of 10 mV.

dx.doi.org/10.1021/ja507297p | J. Am. Chem. Soc. 2014, 136, 13371−13380

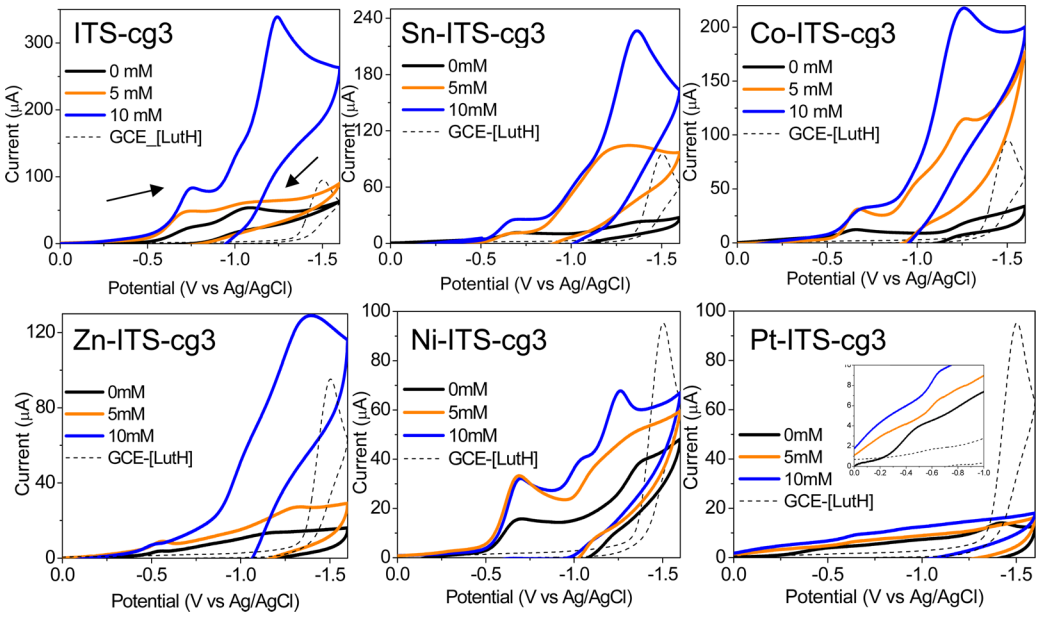

Figure 5. CVs of M-ITS-cg3s and parent ITS-cg3 with $[LutH]^+$ (0, 5, 10 mM) as substrates dissolved in Bu_4NPF_6−CH_3CN solution with a scan rate of 0.06 V/s; GCE, glassy carbon electrode. Inset in the Pt-ITS-cg3 graph is the enlarged view from −0.0 to −0.10 V and displays the reduction potential shifting to more positive values in the presence of $[LutH]^+$.

average proximity (packing density) is altered by the addition of the third metal.

Redox Properties. The Fe_4S_4 structures exhibit well-defined redox activity when the M-ITS-cg3 chalcogels are examined as electrodes with cyclic voltammetry (CV). The sweep of potential in the reductive direction reveals redox waves corresponding to $[Fe_4S_4]^{2+/+}$ core cluster reduction, near −750 mV (vs Ag/AgCl) (Figure 4A; full scan in Supporting Information, Figure S5). These reduction waves are all either quasi-reversible or irreversible (Supporting Information, Figure S5). Compared to the parent chalcogel that contains only $[Fe_4S_4]^{2+}$ cores (ITS-cg3), the reduction potentials of the present chalcogels are shifted to more anodic potentials with decreased current. This shift ranges from 50 to 250 mV (vs Ag/AgCl), with the largest one observed in the Pt-ITS-cg3 sample (Table 1). In our previous study of the binary ITS-cg series using $[SnS_4]^{4-}$, $[Sn_2S_6]^{4-}$, or $[Sn_4S_{10}]^{4-}$, tuning of the chalcogels' properties is achieved by varying the nature of the thiostannate linking block.[38] In the present $M^{2+}/[Fe_4S_4]^{2+}/[Sn_4S_{10}]^{4-}$ chalcogel system, the CV experiments indicate that the M^{2+} cations can also tune the redox properties acting as electron-withdrawing groups, presumably better stabilizing the reduced form of the Fe_4S_4 cluster, in a similar way expected when attaching electron-withdrawing moieties.[40,50−52]

We also investigated the role of M on the charge transport process in these chalcogels using chronocoulometry (CC). We observed that in the M-ITS-cg3s the total charge passed through the chalcogel decreases by ∼66% relative to the parent ITS-cg3 (Figure 4B). This is consistent with the aforementioned overall current decrease in the reduction peak of M-ITS-cg3 samples relative to ITS-cg3. The charge observed up to 10 s decreases in the following sequence: parent ITS-cg3 > Co- > Ni- > Zn- > Sn- > Pt-ITS-cg3. These results suggest that, after the reduction of Fe_4S_4, there is significant *inter*cluster electron hopping in the chalcogel structure and that charge transfer occurs mainly in the same manner in electro-active polymer films.[53] These results are consistent with the notion of the third redox-inactive metal in the chalcogel framework acting to increase the spatial density of the Fe_4S_4 clusters by increasing the average intercluster distance. This lowers the effective electron diffusion coefficient in the gel and consequently the total amount of charge passing through the gel.[54,55] The CC results suggest that the third metals themselves do not participate in transferring charge but rather act as electron-withdrawing moieties onto redox-active Fe_4S_4 clusters, spacing the clusters and thus resulting in different reduction potentials of the clusters. Therefore, the charge transport route in the chalcogel can be controlled with the inclusion of the third metal.

Impedance spectroscopy on M-ITS-cg3 samples supports the results obtained by CC. The resistance and capacitance of M-ITS-cg3 samples are greater than those of the parent ITS-cg3 (Figure 4C and Supporting Information, Table S2). The resistance of M-ITS-cg3s increases overall with the third metal integration (Figure 4C and Supporting Information, Table S2). Particularly, the highest increase is observed in Pt-ITS-cg3, and this accounts for the lower total charge passing through the gel as shown in the CC experiments. The capacitance of Ni-ITS-cg3 and Co-ITS-cg3 chalcogels is higher than that of ITS-cg3 (Supporting Information, Table S2). The decrease in total charge passed and the increases in capacitance and resistance are in accordance with the hypothesis that the Fe_4S_4 clusters are spaced farther apart in the structure compared to the parent ITS-cg3. Thus, a primary role of the incorporated third metal is to effectively modulate the electronic behavior of Fe_4S_4 clusters while serving as a spacer between the clusters.

The redox activity of the Fe_4S_4 clusters and the high porosity and surface area of M-ITS-cg3s (Table 1) afford them key electrocatalytic properties. The electrochemical reduction of protons was studied in the form of lutidinium cations ($[LutH]^+$). The cyclic voltammogram of 2,6-lutidine hydrochloride in acetonitrile at a glassy carbon working electrode shows an irreversible one-electron reduction at −1.50 V vs Ag/AgCl (Figure 5 and Supporting Information, Figure S6). All

dx.doi.org/10.1021/ja507297p | J. Am. Chem. Soc. 2014, 136, 13371−13380

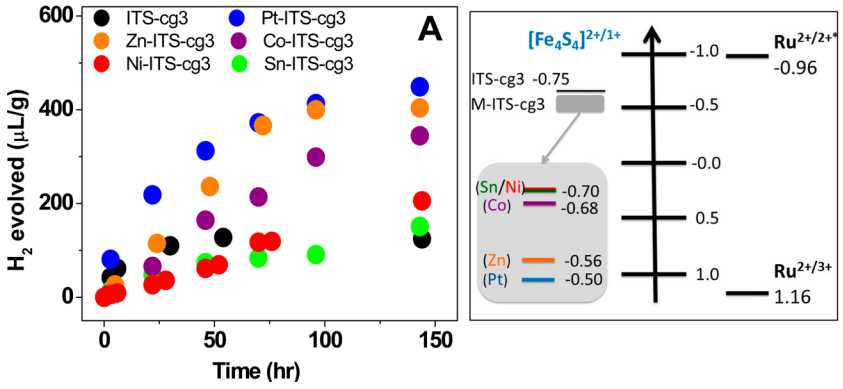

Figure 6. (A) Photochemical hydrogen evolution of $[Ru(bpy)_3]^{2+}$-functionalized M-ITS-cg3 chalcogels, compared with the $[Ru(bpy)_3]^{2+}$-functionalized binary ITS-cg3 sample. The hydrogen output is normalized to the mass of chalcogel present in the experiment. (B) Proposed energy diagram for the $Ru(bpy)_3^{2+}$ in M-ITS-cg3 samples. The energy gradient between $[Fe_4S_4]^{2+/1+}$ and $Ru(bpy)_3^{2+/2+*}$ is greater in M-ITS-cg3 samples than in binary ITS-cg3 and contributes to higher hydrogen output.

redox potentials are given in V vs Ag/AgCl from here. In the absence of $[LutH]^+$, the parent ITS-cg3 exhibits two successive reduction waves corresponding to two redox processes $[Fe_4S_4]^{2+/1+}$ and $[Fe_4S_4]^{1+/0}$ (Figure 5).[25,47] When 5 mM of $[LutH]^+$ is added, the reduction current of $[Fe_4S_4]^{2+/1+}$ increases but the direct electroreduction of $[LutH]^+$ is not observed (Figure 5).[38] However, with the doubled concentration of $[LutH]^+$, the reduction current of $[LutH]^+$ increases significantly at the more positive potential of ~ -1.25 V and the reduction current of $[Fe_4S_4]^{2+/1+}$ increases as well (Figure 5). A similar trend is observed with the M-ITS-cg3 samples, and the direct electroreduction of $[LutH]^+$ is enhanced relative to the bare working electrode.

In the case of Sn-ITS-cg3, the electroreduction of $[LutH]^+$ occurs even with the 5 mM $[LutH]^+$ at -1.36 V (Figure 5). With 10 mM $[LutH]^+$, the shape of the peak becomes more distinct while the height increases, and the reduction current of $[Fe_4S_4]^{2+/1+}$ increases accordingly. With Co-ITS-cg3 and Zn-ITS-cg3 chalcogels, $[LutH]^+$ is lowered to -1.27 and -1.36 V, respectively. Increasing $[LutH]^+$ concentration leads to an increase of the reduction current of $[LutH]^+$ but does not affect that of $[Fe_4S_4]^{2+/1+}$ for both Co-ITS-cg3 and Zn-ITS-cg3. In contrast with these samples, Ni-ITS-cg3 reduces $[LutH]^+$ at -1.26 V, but the reduction current is not enhanced compared to the bare working electrode. The Pt-ITS-cg3 sample does not show any effect on the direct electroreduction of $[LutH]^+$ although its $[Fe_4S_4]^{2+/1+}$ potential shifts toward more positive values and its current increases with the addition of the substrates.

From these results it is clear that the M-ITS-cg3 samples reduce $[LutH]^+$ at significantly more positive potentials. Namely, Sn-, Co-, Zn, and Ni-ITS-cg3 shift the reduction potential to more positive values by ca. 140, 230, 140, and 240 mV, respectively, compared to a bare glassy carbon electrode (Figure 5).

Considering the high resistances observed by impedance spectroscopy experiments, it is expected that not all of the $[Fe_4S_4]$ clusters are active toward the reduction of $[LutH]^+$ because only those near the electrode surface can be redox-activated in a timely manner. Less than 1% of the $[Fe_4S_4]$ clusters of the chalcogels deposited on the electrode are calculated to participate on the initial reduction process based on elemental data, electrode area, and total charge passed through the chalcogel (full calculations in Supporting Information). Therefore, it is promising that the observed electrocatalytic performance of M-ITS-cg3s would improve significantly with the electrode design optimized for a more effective chalcogel contact. These electrochemical observations clearly show significantly decreased overpotential and enhanced current, attesting to the electrocatalytic capability of M-ITS-cg3 for the reduction of $[LutH]^+$.

Photocatalysis. The photocatalytic properties of M-ITS-cg3 were investigated after inserting a molecular photosensitizing moiety into the framework. This was accomplished by taking advantage of the ion-exchangeable countercations ($(C_2H_5)_4N^+$, Ph_4P^+, or K^+) present in the chalcogels to incorporate cationic light-harvesting molecules such as tris(2,2′-bipyridyl)ruthenium(II) ($Ru(bpy)_3^{2+}$).[38] Fourier transform infrared (FTIR) spectroscopy and energy-dispersive spectrometry (EDS) analyses confirm the presence of $Ru(bpy)_3^{2+}$ in the M-ITS-cg3 systems (Supporting Information, Figure S8 and Table S1). The Coulombic attraction between the negatively charged M-ITS-cg3 framework and the cationic $Ru(bpy)_3^{2+}$ leads to an electrostatic attachment proximal to the Fe_4S_4 clusters, setting the stage for electron transfer between the two species.

To evaluate the photochemical H_2-evolving activities of the $Ru(bpy)_3^{2+}$-photosensitized M-ITS-cg3 samples, experiments were conducted under illumination (a 150 W xenon light, $\lambda >$ 300 nm). The photochemical H_2 production experiments were carried out in aqueous solution (4:1 (v/v) acetonitrile–water mixture) sealed in a vial with externally added proton source (500 μmol $[LutH]^+$) and sacrificial electron donors (100 μmol ascorbate). The amounts of H_2 evolved during the experiments were monitored by gas chromatography as described previously.[38] All M-ITS-cg3 samples successfully showed their photochemical H_2-producing ability over a period of 8 days. The amount of H_2 produced gradually increased over 6 days of illumination without degradation in performance and continued until the eighth day when the H_2 evolution started to decrease slowly (Figure 6A). Both the stability of the catalytic chalcogel and the total amount of H_2 evolved are improved in M-ITS-cg3 samples compared to the parent ITS-cg3 material.

For example, the parent Fe_4S_4-only containing ITS-cg systems, including ITS-cg3, often cease evolving H_2 after approximately the fourth day of illumination.[37,38] The M-ITS-cg3 samples showed the enhanced overall stability of Fe_4S_4 clusters, increasing performance well beyond 4 days. The total

dx.doi.org/10.1021/ja507297p | J. Am. Chem. Soc. 2014, 136, 13371–13380

amount of H_2 evolved was the highest in the Pt-ITS-cg3 sample with ~4-fold increase relative to the parent ITS-cg3 (Figure 6A). The activities of the M-ITS-cg3 samples follow the order Pt > Zn > Co > Ni > Sn. It is noted that no appreciable H_2 was produced in the absence of light, of Fe_4S_4, or of $Ru(bpy)_3^{2+}$ in the materials (Supporting Information, Figure S9).[38] The ternary M-ITS-cg3s are clearly superior in activity and stability to the parent binary ITS-cg3 for the light-driven H_2 production.

The improved H_2 evolution by the M-ITS-cg3s can be ascribed to more efficient electron transfer from the photoexcited $Ru(bpy)_3^{2+}$, i.e., $*Ru(bpy)_3^{2+}$, to the Fe_4S_4 clusters due to the more positive reduction potential that was discussed. In our previous studies, including the binary ITS-cg series,[38,39] we have shown that a biomimetic chalcogel with a more positive reduction potential of the redox-active cluster increases the total H_2 yield. This trend suggests that excited $Ru(bpy)_3^{2+}$ is oxidatively quenched by the Fe_4S_4 clusters of the chalcogels. In addition, the calculated free energy for photodriven electron transfer from the photogenerated metal-to-ligand charge-transfer state of $Ru(bpy)_3^{2+}$ to the Fe_4S_4 cluster supports the electron-transfer process between two moieties.[38] Therefore, when the reduction potential of the Fe_4S_4 clusters shifts anodically, oxidative quenching of $*Ru(bpy)_3^{2+}$ becomes more favorable because of the greater driving force for the intermolecular electron transfer.

The proposed energy level diagram of M-ITS-cg3 and $Ru(bpy)_3^{2+}$, shown in Figure 6B, was constructed from the electrochemical and photophysical experiments and compares the relative energies involved in the electron-transfer process. The diagram suggests a more efficient electron transfer in the M-ITS-cg3 systems than in the parent ITS-cg3. Among M-ITS-cg3s, Pt-ITS-cg3 results in the most positive reduction potential for Fe_4S_4 (Figure 6B, Table 1). Consequently, the largest energy difference between the light-harvesting molecule and the Fe_4S_4 clusters in Pt-ITS-cg3 should allow better oxidative quenching of the photoexcited $Ru(bpy)_3^{2+}$. This implies reduced back-recombination and is consistent with the higher H_2 yield observed among the M-ITS-cg3 samples (Figure 6A, B). Correspondingly, the oxidative quenching by M-ITS-cg3s becomes less favorable in the following order: Pt (most) > Zn > Co > Ni > Sn (least). This trend corresponds well with the overall levels of observed H_2 evolution by the M-ITS-cg3s (Figure 6A).

Transient Absorption Spectroscopy. To further investigate the details of the electron-transfer process between $Ru(bpy)_3^{2+}$ and M-ITS-cg3s, we used transient absorption spectroscopy (TA) with an excitation wavelength of 416 nm. The functionalized chalcogels were sonicated in *o*-dichlorobenzene to produce a slurry paste, which was then spuncast onto a glass substrate to give a thin chalcogel film. The Pt- and Co-containing chalcogels were chosen for study with nanosecond TA (nsTA) because of their enhanced H_2-evolving activities. Upon excitation the samples showed ground-state bleaching of $Ru(bpy)_3^{2+}$ at 460 nm and the absence of the typical emissive feature present in the Fe_4S_4 free chalcogel systems and $Ru(bpy)_3^{2+}$ alone sample at 620 nm.[37,38,56] The lifetime of the excited state of $Ru(bpy)_3^{2+}$ at 460 nm is drastically shorter in the M-ITS-cg3s containing $Ru(bpy)_3^{2+}$ than in a solution of the free $Ru(bpy)_3^{2+}$ complex in ethanol (225 ns).[38] The Co-ITS-cg3 displayed a similar time scale (14 ns) to the parent ITS-cg3 (12 ns), whereas Pt-ITS-cg3 showed much more rapid recovery of the $Ru(bpy)_3^{2+}$ ground state (0.6 ns) (Supporting Information, Figure S10). This much faster decay relative to free $Ru(bpy)_3^{2+}$ suggests the presence of interaction between excited $Ru(bpy)_3^{2+}$ and the chalcogels including electron transfer. Specifically, an oxidation pathway for excited $Ru(bpy)_3^{2+}$, involving reduction of Fe_4S_4, is available and is more accessible in Pt-ITS-cg3 than in the parent ITS-cg3 and Co-ITS-cg3.

To further investigate the interaction of $Ru(bpy)_3^{2+}$ and M-ITS-cg3s, the Zn-, Pt-, Co-, Sn-, and parent ITS-cg3 chalcogels, upon illumination we used femtosecond TA (fsTA). Because we cannot monitor the electron directly after the transfer due to the broad, featureless absorption signals observed, it is challenging to determine where the transferred electron population is located. However, based on the energy diagram in Figure 6B and the calculated free energy for the photodriven electron transfer from the photogenerated metal-to-ligand charge transfer, and the fact that all samples showed the quenching of the excited state of $Ru(bpy)_3^{2+}$ (Figure 7), we

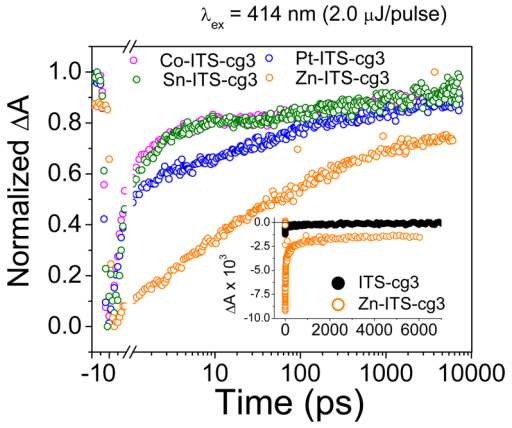

Figure 7. Normalized femtosecond transient absorption at 470 nm following 414 nm excitation of parent ITS-cg3 and M-ITS-cg3 samples; Pt-, Co-, Zn-, and Sn-ITS-cg3. The ground state bleach recovers more quickly in Co-, Sn-, and Pt-ITS cg3 compared to the parent ITS-cg3, illustrating rapid charge transfer to the chalcogel system. The longer lived ground state bleaching in Zn-ITS-cg3 in the inset suggests a longer lived charge separated state in the sample.

expect the following scenarios. The kinetics of free $Ru(bpy)_3^{2+}$ (not in the chalcogel) should be flat on this time scale since the triplet state should live far longer than the ~6 ns instrument window.[37] The observed ground state bleach shows the recombination to the ground state with an accelerated rate and strongly hints the presence of an electron-transfer process where excited $Ru(bpy)_3^{2+}$ molecules undergo electron transfer in M-ITS-cg3s presumably to the Fe_4S_4 clusters, from which they quickly relax back to the ground state (Scheme 2).[37,38] Some of the reduced Fe_4S_4 clusters could survive to produce a charge separated state, $Ru(bpy)_3^{3+}/[Fe_4S_4]^{1+}$ which is expected to contribute to proton reduction to form hydrogen.[38,57] The oxidized $Ru(bpy)_3^{2+}$ species ($Ru(bpy)_3^{3+}$) is then reduced to $Ru(bpy)_3^{2+}$ by the sacrificial electron donor. Especially, the slowest recovery of the $Ru(bpy)_3^{2+}$ bleach observed in Zn-ITS-cg3 suggests the possibility that the charge separated state of the chromophore/donor has a longer lifetime than in ITS-cg3, contributing to the enhanced H_2 output.

Unlike Zn-ITS-cg3, other M-ITS-cg3 samples showed a quicker recovery of the $Ru(bpy)_3^{2+}$ bleach than the parent ITS-cg3. However, on the basis of the energy difference between Fe_4S_4 clusters and excited $Ru(bpy)_3^{2+}$ and the hydrogen output

dx.doi.org/10.1021/ja507297p | J. Am. Chem. Soc. 2014, 136, 13371−13380

Scheme 2. Schematic of intermolecular electron transfer from excited $Ru(bpy)_3^{2+}$ to the parent ITS-cg3 and M-ITS-cg3 chalcogels and the subsequent *inter*cluster electron hopping, illustrating a larger driving force for the *inter*molecular transfer and a longer pathway for *inter*cluster hopping with the inclusion of M^{2+}. (red square=$[Fe_4S_4]^{2+/1+}$,blue circle= M^{2+}; Pt, Zn, Co, Ni, Sn)

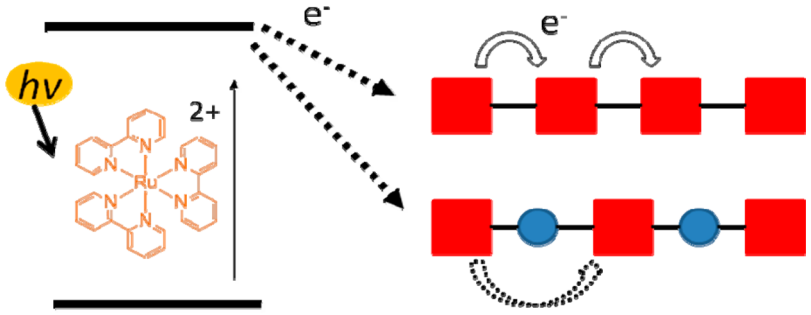

shown in Figure 6, the M-ITS-cg3 samples are expected to show a longer-lived charge-separated state than the parent ITS-cg3. The TA results indicate that there are several factors that govern the intermolecular electron-transfer process between $*Ru(bpy)_3^{2+}$ and the chalcogels. In addition to the relative energies involved in the electron-transfer process between $*Ru(bpy)_3^{2+}$ and the chalcogel, the feasibility of the intercluster electron hopping between Fe_4S_4 units in the chalcogels could contribute to the lifetime of the charge-separated state and, hence, the efficiency of the electron transfer. As discussed in the Mössbauer and CC experiments, the Fe_4S_4 clusters in the M-ITS-cg3 samples are spaced farther apart than in the parent ITS-cg3, and this could impede the electron hopping between the clusters. This separation determines how easily or far the injected electron from $*Ru(bpy)_3^{2+}$ can travel through the chalcogel framework as well as how much cumulative electron transfer is allowed.

In the case of Zn-ITS-cg3, a higher population of the injected electrons from $*Ru(bpy)_3^{2+}$ appears to undergo more extensive diffusion deeper in the structure via intercluster hopping. Note that in this sample, as shown by the enhanced magnetic coupling of Fe_4S_4 clusters observed in the ^{57}Fe Mössbauer spectra, better hopping and better charge separation are expected. For other M-ITS-cg3s, however, the longer average pathway for the intercluster electron hopping yields more shallowly trapped separated electrons on the gel where they can more readily undergo recombination with the $Ru(bpy)_3^{2+}$ state, as depicted in Scheme 2. For Pt-ITS-cg3, a longer spatial distance between the Fe_4S_4 clusters combined with the high resistance compared to ITS-cg3 may facilitate rapid recombination, even though energetically oxidative quenching of the excited $Ru(bpy)_3^{2+}$ is the most favorable as mentioned before.

The amount of light harvesters residing close to a viable acceptor site can determine the efficiency of the intermolecular electron transfer as it can be assumed that only Fe_4S_4 sites that reside close to $Ru(bpy)_3^{2+}$ will be viable acceptors. The M-ITS-cg3 samples exhibit a correlation between the reduction potential of Fe_4S_4 clusters as mediated by M^{2+} and their H_2 photoproduction. The divalent metal M appears to create more desirable photoinduced intermolecular electron transfer by acting as an electron-withdrawing group, allowing more effective oxidative quenching of excited $Ru(bpy)_3^{2+}$, which leads to enhanced photochemical reactivity. Further studies are in progress to determine more accurately the electron-transfer pathway in this complex chalcogel system.

CONCLUSIONS

The M-ITS-cg3s offer a relatively facile way to alter a biomimetic porous material by attaching electron-withdrawing groups on redox-active centers (Fe_4S_4), which are directly and covalently attached to a protective structure using a bottom-up self-assembling process in a one-pot synthesis. The new biomimetic chalcogels introduced in this work utilize the ability of transition metals to tailor the reactivity of Fe_4S_4 reaction centers to achieve light-driven hydrogen production. Moreover, the M-ITS-cg3 samples represent the biomimetic chalcogel's capability to be tailored while maintaining the overall scaffold. The insights generated from this work present a significant advancement in biomimetic catalyst design and emulation of the structure of natural enzymes in real materials. We have shown that the inclusion of a third transition metal into a biomimetic chalcogel system presents a rational reaction-center tuning route to create a targeted biomimetic material with the desired electrochemical and photochemical properties. Integration of metal cations in the Fe_4S_4-containing ITS-cg3 modifies the electrochemical properties of chalcogels and tailors its electrocatalytic ability as seen in the reduction of protons. The incorporation of a third redox-inactive transition metal also results in a more favorable energy landscape for electron transfer between the photoexcited chromophore and the catalytic centers in a superstructure and enhances the photodriven reduction of protons to hydrogen. It also increases the average spacing of the Fe_4S_4 clusters, altering the electron-hopping processes between them. This modification can be used to control the diffusion of reducing equivalents in the chalcogel structure and thus be used to optimize H_2 production. Further, the modular design of this approach allows independent modification of the light-absorbing chromophore, the bridging units, or the catalytic sites to create a diverse class of bioinspired porous materials with catalytic properties

ASSOCIATED CONTENT

Supporting Information

Supporting Information with detailed synthesis procedures, experimental parameters, and characterization techniques of chalcogels is presented. The characterization of the chalcogels (SEM and TEM images, elemental analysis, surface area, specific resistance, and capacitance) and Mössbauer spectra and parameters, full CVs of chalcogels and lutidinium cations, FTIR spectra and elemental analysis of dye-functionalized gels, and nanosecond transient absorption spectra are included. This

material is available free of charge via the Internet at http://pubs.acs.org.

AUTHOR INFORMATION

Corresponding Author

m-kanatzidis@northwestern.edu.

Notes

The authors declare no competing financial interest.

ACKNOWLEDGMENTS

We thank Prof. Joseph Hupp for use of the potentiostat and Dr. Liam C. Palmer for the molecular images in Scheme 1. Electron microscopy and elemental analysis were done through the use of the EPIC facility (NUANCE Center, Northwestern University), which has received support from the MRSEC program (NSF DMR-1121262) at the Materials Research Center, and the Nanoscale Science and Engineering Center (EEC-0118025/003), both programs of the National Science Foundation, the state of Illinois, and Northwestern University. R. M. Y. would like to thank the Camille and Henry Dreyfus Postdoctoral Program in Environmental Chemistry for support. This research was supported as part of the ANSER Center, an Energy Frontier Research Center funded by the U.S. Department of Energy, Office of Science, Office of Basic Energy Sciences, under Award No. DE-SC0001059.

REFERENCES

(1) Moore, G. F.; Sharp, I. D. *J. Phys. Chem. Lett.* **2013**, *4*, 568.
(2) Momirlan, M.; Veziroglu, T. N. *Renewable Sustainable Energy Rev.* **2002**, *6*, 141.
(3) Kim, D. H.; Kim, M. S. *Bioresour. Technol.* **2011**, *102*, 8423.
(4) Cracknell, J. A.; Vincent, K. A.; Armstrong, F. A. *Chem. Rev.* **2008**, *108*, 2439.
(5) Meyer, J. *Cell. Mol. Life Sci.* **2007**, *64*, 1063.
(6) Armstrong, F. A.; Hirst, J. *Proc. Natl. Acad. Sci. U. S. A.* **2011**, *108*, 14049.
(7) Albery, W. J.; Knowles, J. R. *Biochemistry* **1976**, *15*, 5631.
(8) McEvoy, J. P.; Brudvig, G. W. *Chem. Rev.* **2006**, *106*, 4455.
(9) Gust, D.; Moore, T. A.; Moore, A. L. *Acc. Chem. Res.* **2009**, *42*, 1890.
(10) Nelson, N.; Yocum, C. F. In *Annual Review of Plant Biology*; Annual Reviews: Palo Alto, CA, 2006; Vol. *57*, p 521.
(11) Turner, J. A. *Science* **2004**, *305*, 972.
(12) Simmons, T. R.; Artero, V. *Angew. Chem., Int. Ed.* **2013**, *52*, 6143.
(13) Gray, H. B. *Nat. Chem.* **2009**, *1*, 7.
(14) Min, S.; Lu, G. *J. Phys. Chem. C* **2012**, *116*, 25415.
(15) Zong, X.; Wu, G.; Yan, H.; Ma, G.; Shi, J.; Wen, F.; Wang, L.; Li, C. *J. Phys. Chem. C* **2010**, *114*, 1963.
(16) Le Goff, A.; Artero, V.; Jousselme, B.; Tran, P. D.; Guillet, N.; Metaye, R.; Fihri, A.; Palacin, S.; Fontecave, M. *Science* **2009**, *326*, 1384.
(17) Tard, C.; Liu, X. M.; Ibrahim, S. K.; Bruschi, M.; De Gioia, L.; Davies, S. C.; Yang, X.; Wang, L. S.; Sawers, G.; Pickett, C. J. *Nature* **2005**, *433*, 610.
(18) Sun, L. C.; Akermark, B.; Ott, S. *Coord. Chem. Rev.* **2005**, *249*, 1653.
(19) Evans, D. J.; Pickett, C. J. *Chem. Soc. Rev.* **2003**, *32*, 268.
(20) Maeda, K.; Teramura, K.; Lu, D. L.; Takata, T.; Saito, N.; Inoue, Y.; Domen, K. *Nature* **2006**, *440*, 295.
(21) Barton, B. E.; Rauchfuss, T. B. *J. Am. Chem. Soc.* **2010**, *132*, 14877.
(22) Darensbourg, M. Y.; Weigand, W. *Eur. J. Inorg. Chem.* **2011**, 917.
(23) Hou, Y. D.; Abrams, B. L.; Vesborg, P. C. K.; Bjorketun, M. E.; Herbst, K.; Bech, L.; Setti, A. M.; Damsgaard, C. D.; Pedersen, T.; Hansen, O.; Rossmeisl, J.; Dahl, S.; Norskov, J. K.; Chorkendorff, I. *Nat. Mater.* **2011**, *10*, 434.
(24) Coucouvanis, D.; Kanatzidis, M.; Simhon, E.; Baenziger, N. C. *J. Am. Chem. Soc.* **1982**, *104*, 1874.
(25) Kanatzidis, M. G.; Coucouvanis, D.; Simopoulos, A.; Kostikas, A.; Papaefthymiou, V. *J. Am. Chem. Soc.* **1985**, *107*, 4925.
(26) Gloaguen, F.; Lawrence, J. D.; Rauchfuss, T. B. *J. Am. Chem. Soc.* **2001**, *123*, 9476.
(27) Mascharak, P. K.; Papaefthymiou, G. C.; Armstrong, W. H.; Foner, S.; Frankel, R. B.; Holm, R. H. *Inorg. Chem.* **1983**, *22*, 2851.
(28) Gloaguen, F.; Lawrence, J. D.; Rauchfuss, T. B. *J. Am. Chem. Soc.* **2001**, *123*, 9476.
(29) Schmidt, M.; Contakes, S. M.; Rauchfuss, T. B. *J. Am. Chem. Soc.* **1999**, *121*, 9736.
(30) Ihara, M.; Nishihara, H.; Yoon, K. S.; Lenz, O.; Friedrich, B.; Nakamoto, H.; Kojima, K.; Honma, D.; Kamachi, T.; Okura, I. *Photochem. Photobiol.* **2006**, *82*, 676.
(31) Tye, J. W.; Hall, M. B.; Darensbourg, M. Y. *Proc. Natl. Acad. Sci. U. S. A.* **2005**, *102*, 16911.
(32) Wilson, A. D.; Newell, R. H.; McNevin, M. J.; Muckerman, J. T.; DuBois, M. R.; DuBois, D. L. *J. Am. Chem. Soc.* **2006**, *128*, 358.
(33) Smith, S. E.; Yang, J. Y.; DuBois, D. L.; Bullock, R. M. *Angew. Chem., Int. Ed.* **2012**, *51*, 3152.
(34) Camara, J. M.; Rauchfuss, T. B. *Nat. Chem.* **2012**, *4*, 26.
(35) Heine, D.; Pietsch, C.; Schubert, U. S.; Weigand, W. *J. Polym. Sci., Polym. Chem.* **2013**, *51*, 2171.
(36) Gray, H. B.; Malmstrom, B. G.; Williams, R. J. P. *J. Biol. Inorg. Chem.* **2000**, *5*, 551.
(37) Yuhas, B. D.; Smeigh, A. L.; Samuel, A. P. S.; Shim, Y.; Bag, S.; Douvalis, A. P.; Wasielewski, M. R.; Kanatzidis, M. G. *J. Am. Chem. Soc.* **2011**, *133*, 7252.
(38) Shim, Y.; Yuhas, B. D.; Dyar, S. M.; Smeigh, A. L.; Douvalis, A. P.; Wasielewski, M. R.; Kanatzidis, M. G. *J. Am. Chem. Soc.* **2013**, *135*, 2330.
(39) Yuhas, B. D.; Smeigh, A. L.; Douvalis, A. P.; Wasielewski, M. R.; Kanatzidis, M. G. *J. Am. Chem. Soc.* **2012**, *134*, 10353.
(40) Yuhas, B. D.; Prasittichai, C.; Hupp, J. T.; Kanatzidis, M. G. *J. Am. Chem. Soc.* **2011**, *133*, 15854.
(41) Green, K. N.; Hess, J. L.; Thomas, C. M.; Darensbourg, M. Y. *Dalton Trans.* **2009**, 4344.
(42) (a) Bag, S.; Trikalitis, P. N.; Chupas, P. J.; Armatas, G. S.; Kanatzidis, M. G. *Science* **2007**, *317*, 490. (b) Kanatzidis, M. G. *Advanced Materials* **2007**, *19*, 1165.
(43) Shafaei-Fallah, M.; He, J. Q.; Rothenberger, A.; Kanatzidis, M. G. *J. Am. Chem. Soc.* **2011**, *133*, 1200.
(44) Vincent, K. A.; Parkin, A.; Armstrong, F. A. *Chem. Rev.* **2007**, *107*, 4366.
(45) Moulis, J. M.; Meyer, J. *Biochemistry* **1982**, *21*, 4762.
(46) Wong, G. B.; Bobrik, M. A.; Holm, R. H. *Inorg. Chem.* **1978**, *17*, 578.
(47) Coucouvanis, D.; Kanatzidis, M. G.; Dunham, W. R.; Hagen, W. R. *J. Am. Chem. Soc.* **1984**, *106*, 7998.
(48) Kanatzidis, M. G.; Baenziger, N. C.; Coucouvanis, D.; Simopoulos, A.; Kostikas, A. *J. Am. Chem. Soc.* **1984**, *106*, 4500.
(49) Chakrabarti, M.; Deng, L.; Holm, R. H.; Munck, E.; Bominaar, E. L. *Inorg. Chem.* **2009**, *48*, 2735.
(50) Zhou, C. Y.; Raebiger, J. W.; Segal, B. M.; Holm, R. H. *Inorg. Chim. Acta* **2000**, *300*, 892.
(51) Jensen, K. P.; Ooi, B. L.; Christensen, H. E. M. *J. Phys. Chem. A* **2008**, *112*, 12829.
(52) Zhu, N. Y.; Appelt, R.; Vahrenkamp, H. *J. Organomet. Chem.* **1998**, *565*, 187.
(53) Ak, M.; Toppare, L. *Mater. Chem. Phys.* **2009**, *114*, 789.
(54) Daum, P.; Lenhard, J. R.; Rolison, D.; Murray, R. W. *J. Am. Chem. Soc.* **1980**, *102*, 4649.
(55) Atta, N. F.; Galal, A.; Ali, S. M. *Int. J. Electrochem. Sci.* **2012**, *7*, 785.
(56) Kitamura, N.; Obata, R.; Kim, H. B.; Tazuke, S. *J. Phys. Chem.* **1989**, *93*, 5764.

(57) Hollmann, D.; Karnahl, M.; Tschierlei, S.; Kailasam, K.; Schneider, M.; Radnik, J.; Grabow, K.; Bentrup, U.; Junge, H.; Beller, M.; Lochbrunner, S.; Thomas, A.; Brückner, A. *Chem. Mater.* **2014**, *26*, 1727.